JARS Journal of Applied Remote Sensing

RESEARCH PAPER

Academic development and space operations of a multispectral imaging payload for 1U CubeSats

Luis Zea,* Aldo Aguilar-Nadalini, Marvin Martínez, Johan Birnie, Emilio Miranda, Fredy España, Kuk Chung, Dan Álvarez, José Antonio Bagur, Carlo Estrada, Rony Herrarte, and Víctor Ayerdi*

Universidad del Valle de Guatemala, Guatemala City, Guatemala

ABSTRACT. Multispectral remote sensing can enable myriad applications, including land cover change mapping and monitoring of vegetation activity and forest fires, to name a few. Although the acquisition of multispectral remote sensing data could empower developing countries toward better management of their natural resources, acquiring this type of data is not trivial. To assess a potential solution to lowering the barrier to entry for these types of missions, Quetzal-1, a 1U CubeSat and Guatemala's first satellite, tested a payload prototype on a relatively lower budget. This prototype's approach was based on housing a series of bandpass filters on a carousel that was rotated by a piezoelectric motor, so that a sensor could acquire data at different wavelengths. We provide a guideline for replicating this prototype (including engineering drawings) and the logic behind its design, describing how the data collection wavelengths were selected and introducing key optics and photography concepts needed for the optimal setup of the sensor, lens, and filters. The governing software architecture and preflight testing (including computer-based simulation and vibration testing) is also described. On-orbit performance parameters, such as power consumption, are provided and contrasted to preflight test results, as well as the impact of payload operations on the satellite's attitude. Quetzal-1's piezoelectric motor rotated more than 1800 times in space, and the payload imaged hurricane Iota as it was hitting Guatemala. Although the development of this payload is still work in progress, the lessons learned from the development and operation in space of this first prototype can serve other teams designing their own multispectral imaging CubeSat missions, which by changing the light filters may implement different remote sensing applications.

Keywords: remote sensing; nanosatellite; developing countries

Paper 230173G received Apr. 20, 2023; revised Oct. 20, 2023; accepted Nov. 15, 2023; published Dec. 6, 2023.

1 Introduction

Universidad del Valle de Guatemala's (UVG) developed Guatemala's first satellite, Quetzal-1, a 1U CubeSat, as an academic project for undergraduate students. Its potential missions were quantitatively compared via a methodology that considered their feasibility of being implemented on a CubeSat platform, relevance to institutional and national priorities, expected scientific and technical output, required resources, and programmatic risks.[1] From this study, water color (quality)

*Address all correspondence to Luis Zea, lpzea@uvg.edu.gt; Víctor Ayerdi, vhayerdi@uvg.edu.gt

monitoring was selected as the satellite's ultimate technical mission, for which a prototype payload was to be developed and tested on orbit. However, the overarching goals of the Quetzal-1 project were to (i) open the field of space science and technology in Guatemala, (ii) develop the country's human capital by developing and operating a satellite in-house, (iii) enable the independent acquisition of remote sensing data for natural resource management, and, most importantly, (iv) to inspire the next generation into following science, technology, engineering, and mathematics careers. To achieve this, Quetzal-1's specific mission was to test whether our team could develop and operate a payload prototype based on a piezoelectric motor rotating a carousel with light filters to acquire images at specific wavelengths.

Quetzal-1 was selected by the United Nations Office for Outer Space Affairs and the Japan Aerospace Exploration Agency (JAXA) as the winner of the second round of their KiboCUBE Program, which covered the launch to the International Space Station (ISS) and deployment from its Kibo module, which took place on March 7, 2020, and April 28, 2020, respectively.[2] The systems engineering approaches implemented on this project are described by Martínez et al.,[3] the electrical power system (EPS) by Aguilar-Nadalini et al.,[4] the Attitude Determination and Control System (ADCS) by Alvarez et al.,[5] the structure's finite-element analysis (FEA) by Birnie et al. (internal communication), and the command and data handling systems (CDHS) by Chung et al. (internal communication). This manuscript focuses on Quetzal-1's payload, which consisted of an assembly that allowed a sensor to collect reflected solar radiation at different wavelengths via a carousel that housed four bandpass filters, which was rotated by a piezoelectric motor (Fig. 1). This paper describes the requirements regarding the satellite's water color monitoring technical mission (Sec. 2), the payload design and development in a per-component fashion, interfaces with other subsystems, and governing software (Sec. 3), preflight testing (Sec. 4), on-orbit performance and results (Sec. 5), finishing with a discussion of the development process and results, and conclusions and recommendations for other teams designing their own multispectral imaging CubeSat payload (Sec. 6).

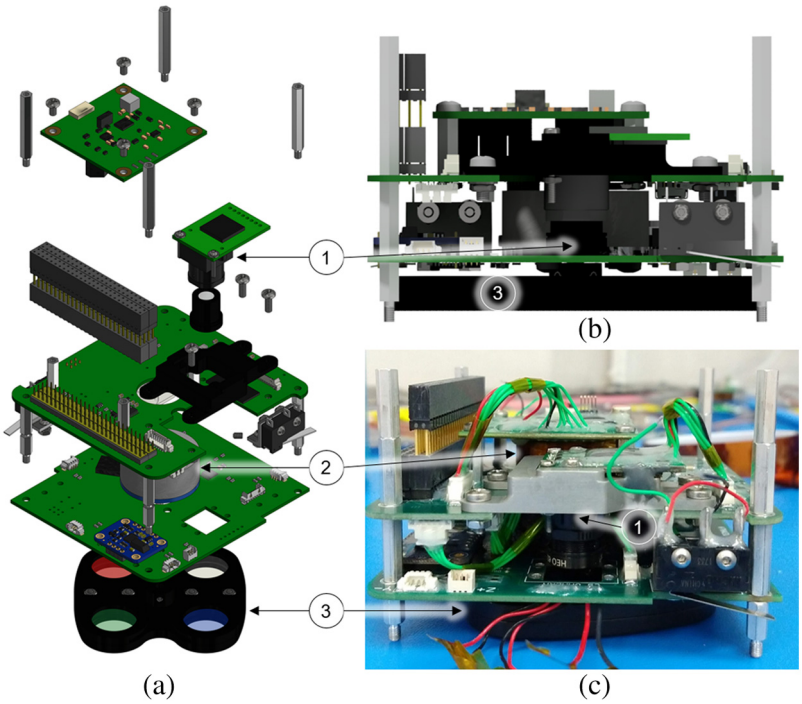

Fig. 1 Quetzal-1's payload essential components: (1) sensor for image collection, (2) a piezoelectric motor used to rotate, and (3) a carousel that housed four bandpass filters. (a) Isometric CAD model, (b) side CAD view, and (c) flight hardware integrated for characterization testing prior to launch.

2 Requirements and Constraints

2.1 Driven by the CubeSat Standard, Other Systems, and Implementation for Flight

The CubeSat standard sets limits for mass and volume to 1.33 kg and a 10-cm per side, respectively, per cubic unit (U); the satellite can be composed of one or more of these units (Quetzal-1 was a 1U CubeSat).[6] All of the satellite's subsystems-structure, EPS, ADCS, on-board computer (OBC), and other components required by the CDHS, as well as the payload must fit within these volume and mass constraints. A hierarchical approach was taken to Quetzal-1's development in that a baseline design was produced for each subsystem, leaving the payload for last—mostly due to limited number of students available for this academic project. Hence, each of the systems-imposed requirements and constraints on the payload based on their own characteristics, capabilities, and limitations.

From the EPS perspective, these included that the motor could not require more than 1 A, 5.5 V, and 14.8 W of current, voltage, or power, respectively, and that the camera could not require more than 3.3 V.[4] The ADCS, in turn, limited the motor's torque to reduce the rotational disturbances introduced into the system. Similarly, and due to the passive nature of Quetzal-1's ADCS, it was required that the motor accelerated and decelerated at the same rate to induce a net torque equal to zero over the Z axis of the satellite (around which the payload's light filter carousel rotated).[5] If the motor-induced torque were to be different than zero, the satellite's rotational energy would increase with each rotation of the carousel. Additionally, it was important to minimize the electromagnetic characteristics of the motor to be used. Typical direct current (DC) servo and most stepper motors contain permanent magnets that enable operation, which would potentially modify the alignment of the passive ADCS with Earth's magnetic field. Note that a predictable alignment was important, as it was necessary to align the camera's boresight to Earth at the desired locations to take relevant images.[5]

This mission was constrained to using the UHF band due to its amateur radio application and, most importantly, regulatory framework limitations in Guatemala. This consequently constrained how much data (file size and amount of files) could be transmitted down to the GCS during an overflight. Furthermore, the selection of the OBC (GOMSpace, Cat. No. NanoMind A3200) generated a series of requirements and constraints on the payload. These included that the motor control interface could not exceed nine general purpose input/output (GPIO) pins of the OBC and that the communication interface with the camera had to be I2C, CAN, SPI, or UART.

The launch and space environment, as well as the deployment of Quetzal-1 from the ISS, generated additional requirements that directly impacted the payload design. These included launch quasistatic loads and overall random vibration of 18.1 g and 4.825 Grms, respectively, and a volume to exhaust port area ratio of <50.8 m.[6] Additionally, component materials had to have an "A" rating on NASA's Materials and Processes Technical Information System[7] (which translated into not being able to use lubricants of special impact for motor selection). The rationale for this is that out-gassing (the release of gases trapped within a solid when exposed to a vacuum) can result in condensation on the smooth optical surfaces (glass lens and light filters). No material with a total mass loss above 1.0% or a collected volatile condensable material above 0.1% could be used on the payload or in the satellite in general.[6] Finally, on-orbit operations at an ISS-like orbit (~420 km altitude, 51.6 deg inclination) required that the satellite components could operate in a −15°C to +60°C temperature range in a near vacuum.[6]

2.2 Driven by the Water Color Monitoring Mission

The selection of Quetzal-1 payload's data collection wavelengths is here described in the context of its water color monitoring mission. However, by changing the commercial-off-the-shelf (COTS) bandpass filters, others may implement the same or equivalent payload to serve different remote sensing applications in 1U or larger CubeSats. The initial step to determine the requirements imposed by the water color monitoring mission, per se, was to identify the number of channels (wavelengths where images are acquired) that were needed to enable water quality characterization from space. Specific wavelengths provide information on different constituents in the water, stressing the importance of the appropriate selection of the sensor's channels. Mertes

et al.,[8] a review of over 1000 journal publications, books, and reports focused on rivers and lakes, was used as the guiding reference for this purpose. Remote sensing enables the estimation of several water quality properties, including colored dissolved organic matter (CDOM), concentration of total suspended matter, chlorophyll-a content, and phycocyanin, a pigment indicative of the presence of cyanobacteria, among others. The presence of algae (and chlorophyll in general) in water results in changes in absorption, mostly between 400 and 500 nm, and between 600 to 700 nm wavelength range. In general, the range of 400 to 700 nm is known as the photosynthetically active radiation range.[8] A literature survey showed that, originally, most of the algorithms—equations developed to quantify a parameter from images or other types of data—for chlorophyll concentration determination depended on the ratio of two bands. However, newer algorithms that used three bands have shown to increase algorithm tolerance to atmospheric correction, especially important for short wavelengths.[9] For example, IOCCG[10] indicate that the OCM sensor on board the Indian satellite IRS-P4 uses data from the 768 and 867 nm wavelengths for atmospheric corrections. Hu et al.[11] presented an algorithm used on SeaWiFS data using the 443, 555, and 670 nm wavelengths. It is suggested that this three-band approach increases performance, especially for low chlorophyll concentrations (<0.25 mg/m^3). Similarly, the use of red (~650 nm) and/or near-infrared (NIR) (>700 nm) bands help avoid CDOM contamination problems.[9] Hence, some algorithms have been based on the use of four bands.[9] Table 3 (Appendix A) summarizes the functional parameters of sensors used for water color monitoring applications. Starting with the coastal zone color scanner (CZCS) sensor onboard the Nimbus-7 satellite (launched in 1978), these devices have been used for purposes beyond chlorophyll-a concentration determination, and this is reflected in their use of multiple channels (e.g., detecting oil spills or assessing fishing resources).

Data from the CZCS was used to calculate chlorophyll-a concentration through "blue-green band ratio" models, where the reflectance at 550 nm was compared to that at 443 or 520 nm. In this case, the 550 nm band is used as a reference, as it is minimally affected by chlorophyll-a concentration.[9] Table 3 shows that data collected at 443 nm has been a common numerator among the analyzed algorithms. Similarly, data acquired at a channel between 547 and 560 nm have been used as the denominator for the blue-green band ratio among these algorithms. Additionally, three-channel algorithms used to determine chlorophyll-a concentration from SeaWiFS data utilized the 670 nm wavelength.[11] As indicated by Hu and Campbell,[9] this wavelength helps in differentiating CDOM from chlorophyll-a in the collected light.

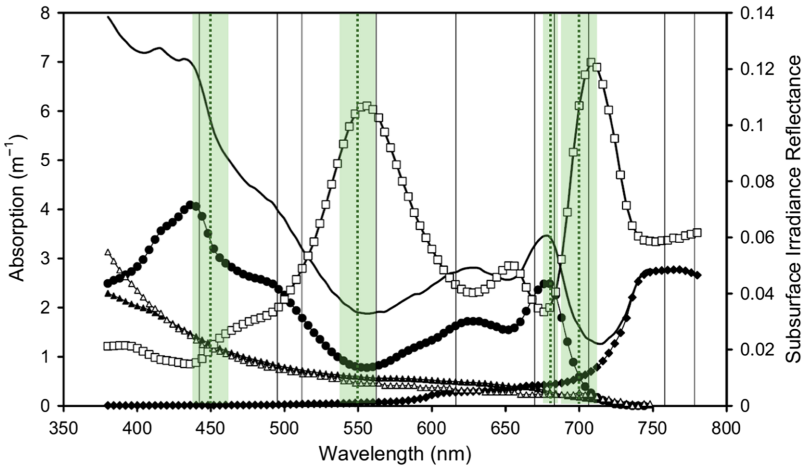

Fig. 2 Adapted from Gons et al.[12]. Line without symbols, total absorption coefficient; solid circles, plankton biomass absorption; open triangles, gilvin; and solid diamonds, water. The subsurface irradiance reflectance is shown with open squares and uses the right axis. Solid vertical lines were placed over the MERIS bands. Dotted green vertical lines represent the center of Quetzal-1's bands: 450, 550, 680, and 700 nm. The green boxes around them represent the bandpass for each of the four light filters (25 nm in all cases except for the 680 nm filter, for which it was 10 nm). Adapted with permission from Ref. 12, copyright (2005).

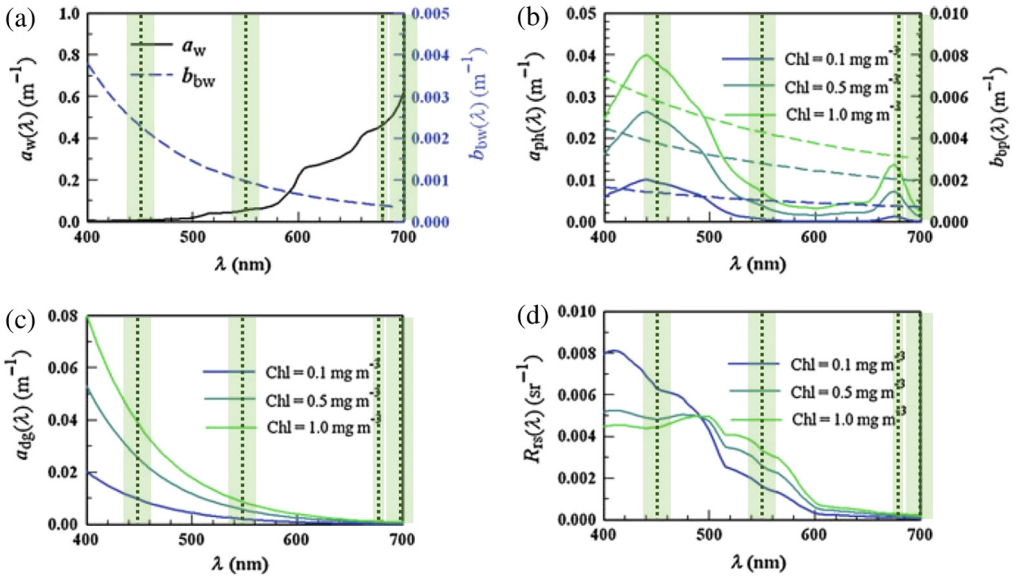

Fig. 3 (a) Water and (b) phytoplankton (chlorophyll-a) absorptivity (solid lines) and particulate backscattering coefficient (dotted lines) as a function of wavelength; (c) CDOM absorptivity, which can help differentiate in between phytoplankton and other organic material; and (d) reflectance. These figures show the importance of the channels selected for Quetzal-1 (450, 550, 680, and 700 nm, with green bands indicating their respective bandpasses) for determining chlorophyll-a concentration. Adapted with permission from Ref. 9, copyright (2014).

In conclusion, a literature survey on algorithms used to determine chlorophyll-a concentration in lakes, and on the sensors used in satellites with this objective, showed channels centered at (a) the 443 nm and (b) in between 547 and 560 nm as numerators and denominators, respectively. The use of a third channel around the red (~650 nm) and/or NIR (>700 nm) bands help to differentiate signals from CDOM and chlorophyll-a.[9] Hence, and to facilitate the development of an algorithm for Quetzal-1's data, the three channels used in the SeaWiFS sensors—443, 555, and 670 nm—were chosen as the water color monitoring mission specific requirements. Additionally, as nature of the hardware design allowing for data acquisition at four wavelengths (see Sec. 3.1), 700 nm was included to acquire additional data, potentially extendable to land applications. The wavelengths implemented on the satellite's payload varied by a few nanometers in most cases as described in Sec. 3.1 based on which light filters were commercially available. Figures 2 and 3 show the wavelength location and bandpass (range of wavelengths into which it allows photons to be transmitted) of Quetzal-1's light filters in the electromagnetic spectrum in the context of chlorophyll-a characterization.

3 Design and Development

3.1 Light Filter Carousel

Based on the selection of wavelengths for data acquisition, light filters were chosen taking into account their dimensions, mass, closeness to target wavelength, bandpass, and price. Hence, for the target 443, 555, 670, and 700 nm, light filters centered at 450, 550, 680, and 700 nm were selected, respectively (each with a 25 nm bandpass with the exception of the 680 nm filter, for which it was 10 nm) (Edmund Optics, Cat. Nos. 86-653, 86-655, 86-571, and 86-658, respectively). This is summarized in Table 1.

Different approaches were considered to implement these light filters and the overall multispectral imaging payload within the limitations and constraints of a 1U CubeSat bus, including having multiple cameras (each with a designated light filter), using a "stack" held by an axle, and a "carousel" or disk holding the light filters (changed via a motor). Based on the volume, mass, torque and power needed for implementation, cost, and complexity of spaceflight operations, the light filter carousel was chosen via a trade study. Additionally, the carousel approach enabled the inclusion of a fourth light filter given its dimensions. Al7075 was chosen as the carousel material,

Table 1 Summary of the wavelengths selected for the water color monitoring mission of the payload prototype, and their rationale for selection. Desired and actual wavelengths vary due to COTS hardware availability.

Desired wavelength (nm)	Actual wavelength (nm)	Function
443	450	To quantify presence of chlorophyll-a[8]
555	550	Reference bandwidth, as it is minimally affected by chlorophyll-a concentration[9]
670	680	To differentiate between chlorophyll-a and CDOM[9]
700	700	

which per requirements, this (and all other) aluminum components were hard anodized following specifications by MIL-A-8625 type 3 class 1, which formed a coating with a thickness of at least 10 μm; in the case of the carousel specifically, it was black-anodized to minimize reflections. The carousel was composed of three main parts: two "top" and one "bottom" plates (see items 1 and 2, respectively, in Fig. 4). These plates housed the light filters (shown in Fig. 4 as items 8 to 11) using Viton O-rings (The O-Ring Store LLC, Cat. No. V1.00X021.5) (one per light filter) to

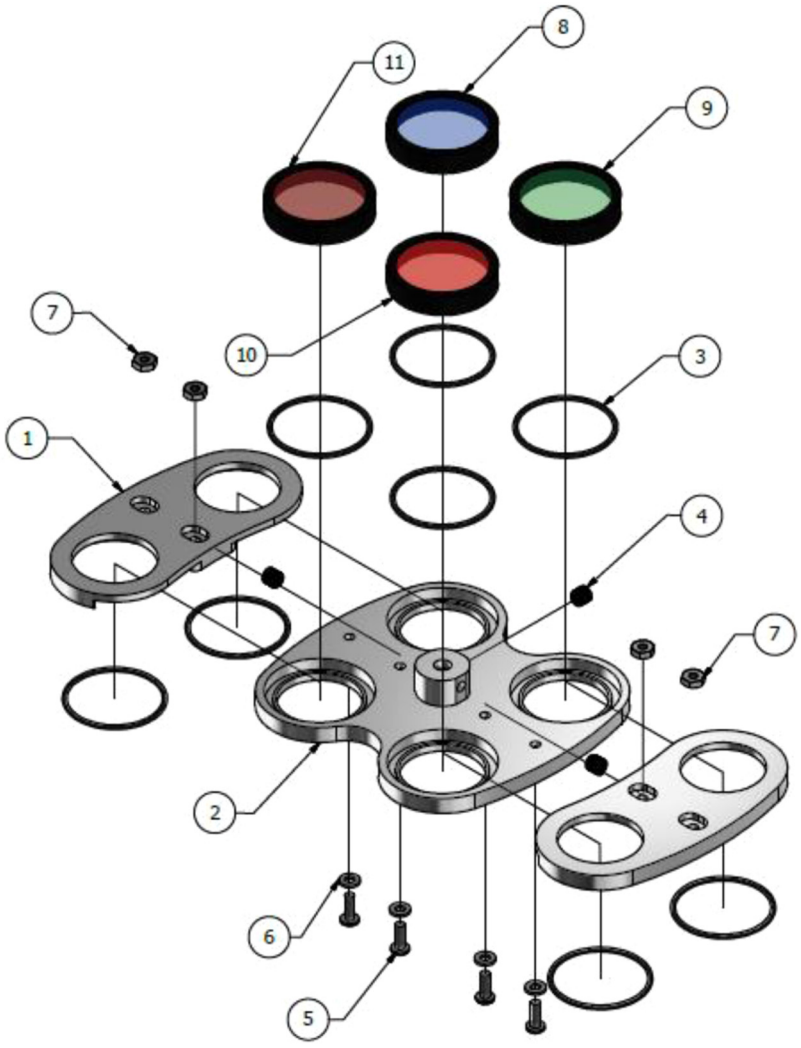

Fig. 4 Exploded view of Quetzal-1's light filter carousel: (1) top plates (×2), (2) bottom plate, (3) O-rings (×4), (4) to (7) fasteners, and (8) to (11) light filters. Engineering drawings are included as an appendix.

dampen the launch vibrations that could otherwise jeopardize these glass components. The carousel's engineering drawings are included as an appendix and the computer assisted design (CAD) models can be downloaded from Ref. 13.

3.2 Motor

To rotate the light filter carousel so that a single camera could be used, different types of motors—DC, stepper, continuous rotation servo, and piezoelectric—were assessed. As described in Sec. 2.1, the requirements that no electromagnetic motors or lubricants be used impacted motor selection. Piezoelectric motors convert an electrical field into mechanical strain, which in turn, translates into motion using fewer parts compared to their electromagnetic counterparts, while being free of lubricants. Hence, it was determined that a piezoelectric motor was ideal for this application, with the caveat that no previous use of these types of devices on CubeSats could be found. A trade study was used to select the specific piezoelectric motor to use in spaceflight. The variables considered for the selection included volume (dimensions), power consumption, operational temperature range, whether it had spaceflight heritage (for risk mitigation), mass, angular accuracy, acceleration profile, and cost. TEKCELEO's WLG-30 model was chosen through this process, due to the following beneficial characteristics:

- Its mass was low and the operational temperature range exceeded what was needed for operations in lower-Earth orbit with close to no insulation (as was the case of Quetzal-1).
- The carousel positioning accuracy requirement was ≤ 0.13 deg to adequately align the lens of the camera to the light filters, and the WLG-30 piezoelectric motor provided an accuracy of 0.01 deg.
- The WLG-30 piezoelectric motor was nonmagnetic, in contrast to electromagnetic motors, which eliminated the possibility of magnetic interference with the passive magnetic attitude control system implemented for Quetzal-1.[2]
- The piezoelectric motor provided high-holding torque and low rotor inertia that enabled fast response of the carousel system. This allowed fast execution of the picture capture process while flying over Guatemala at orbital speed.

The main drawbacks included the lack of spaceflight heritage and the need for an additional 7.5 V power rail dedicated to the motor, which had to be implemented on the payload circuit board. Otherwise, the selection of a piezoelectric motor proved to be the best alternative to reduce mass, volume, and electromagnetic interference, while also guaranteeing a <0.13 deg carousel positioning accuracy and fast operating response.

This motor included a driver, which allowed to control the piezoelectric device in a simple fashion since its inputs were GPIOs. Aside from the power on and off pins, the driver had pins to select the direction of rotation (clockwise or counterclockwise), an increment pin (to count steps), and an index pin (to count full rotations).

3.3 Camera

Requirements for the camera selection included interfacing with the OBC and EPS, maximum peak and nominal power consumption, volume (dimensions), mass, operational temperature range, capability to store images, and generated file type and size. Given that Quetzal-1's payload was a prototype—for test demonstration, verification, and subsequent maturation—and not designed to be used for systematic water color monitoring data acquisition, no spatial resolution requirements were imposed—but were considered—during the camera selection process. Different types of sensors were analyzed for this mission, including red–green–blue (RGB) sensors, multispectral cameras, and monochromatic sensors. RGBs are the simplest to integrate but selectively receive light at those three wavelengths, exclusively. Multispectral cameras with Bayer patterns are ideal as they can be procured to acquire data specifically in the wavelengths of the mission's interest; however, these types of sensors can be two or more orders of magnitude more expensive (as well as larger and more power-consuming), reasons for which they could not be further considered for the Quetzal-1 satellite. Finally, monochromatic sensors are ideal to be used behind light filters, such as the ones housed in this payload's carousel. These types of sensors do not have a color filter array, i.e., each pixel receives light through the whole range

of wavelengths the sensor is set up to receive (e.g., 350 to 950 nm), thus the light-filtering function is achieved with the light filters. Through the design and development phases of the Quetzal-1 project, a monochromatic camera was included. However, the camera arrived half a year after expected, it had different dimensions and mass than what was conveyed in the drawings, and most importantly, it did not have the communication bus that was advertised, all of which required the swift selection of a new device—while all other modules were ready to transition to the integrated testing phase and with handover date prior to launch a few months away. Given its open-source nature, low complexity, and compatibility with the other, already established satellite systems (namely, the other payload's components), Arducam's OV5642 camera was the new selection for flight. This device uses a 5 MP complementary metal oxide semiconductor 2592×1944 array size, $1.4\ \mu\text{m} \times 1.4\ \mu\text{m}$ pixel size, 63-pin CSP3 digital image sensor (OmniVision Technologies Inc., Cat. No. OV05642-A63A) and was launched set up with autoexposure control (AEC), autogain control, auto white balance, autofocus control, black and white, and JPG compression. Although this was a deviation from the original payload design, it enabled to continue towards launch and testing of the prototype approach based on a piezoelectric motor rotating a light filter carousel in a 1U CubeSat. According to the manufacturer, the minimum and maximum exposure times for this family of sensors are 53.39 μs and 66.63 ms, respectively, and saving times as short as 816 ms.[14] Ultimately, captured images were stored in an SD memory.

3.4 Optical Design and Lens

In order to design an imaging payload, several key optics and photography concepts need to be considered, which are described here and noted in italics, and graphically represented in Fig. 8 (Appendix B). The distance between the lens and the sensor depends on the system's focal length. This is the distance from the point where light rays converge to form an image, to the digital sensor and has a role on the area that is captured; the longer the focal length is, the narrower the angle of view and therefore the higher the magnification is. The focal length is defined by the following equation:

$$\frac{1}{f} = \frac{1}{u} + \frac{1}{v}, \tag{1}$$

where f is the focal length, u is the distance to the target, and v is the distance between the lens and the sensor.[15] More specifically, back focal length is the distance between the last optical surface of a lens and the location of the sensor (important to ensure appropriate focus). Additionally, field of view is the surface area that can be imaged and processed. The equation for the angular field of view is

$$\text{AFOV} = 2 \times \tan^{-1}\left(\frac{\text{FOV}_{\text{horizontal}}}{2 \cdot \text{WD}}\right), \tag{2}$$

where WD is the working distance in length (versus angle) units, and FOV is the horizontal field of view.[16] All of these parameters play a role on the payload's spatial resolution (surface area covered by one pixel).

The F number is a measure of the lens opening and amount of light that goes through a lens (inversely proportional to aperture) and impacts focus and depth of field (range of distances in which objects are still in focus). In the case of remote sensing applications, it is important to have a high $F\#$ (small aperture), as it yields a greater depth of field.[16,17] The $F\#$ can be calculated as the ratio of the focal length and the lens' diameter d:

$$F\# = \frac{f}{d}. \tag{3}$$

For a sensor to capture an entire image and not just part of it, it is recommended to select a lens larger than the sensor size optical format—approximately the diagonal length of the sensor multiplied by 2/3. For example, a sensor with a ¼ in. optical format could be used with a 1/3 in. sensor. If the lens and the sensor's optical format are of the same dimension, some optical problems as dark or blur edged or copped areas on the image may occur.[18] Another important parameter is the ISO value, a measure of the sensor's ability to capture (or sensitivity to) light.[19]

A brighter light environment requires a lower ISO number or a higher shutter speed—how long the shutter is open, exposing the sensor to light—and is usually used under bright conditions (e.g., sunlight or for long-exposure photos). Conversely, low-light environments require slower shutter speeds are a higher ISO value. Something to consider is that high ISO numbers tend to increase the noise level in the image.[19] To better understand how the ISO number, the shutter speed, and the aperture interact between each other, readers are encouraged to seek more information on the "exposure triangle."

Finally, the type of global shutter or rolling shutter needs to be considered. The prior [common in charge-couple device sensors] exposes every pixel to the light simultaneously, resulting in slower transfer rates. The latter exposes one column or row of pixels at a time, resulting in faster transfer rates but can potentially result in distortion when capturing a fast-moving target.[20] In addition to the optical design-driven requirements, the lens selection took into account the space available to the overall payload subsystem, including the distance between the camera and the light filter carousel and the light filters' dimensions. From this, the lens integrated to the selected camera (DLSCorp., Cat. No. M2508ZH02) was confirmed to be appropriate for this mission's application with its 1/2 in. maximum sensor format, $f/2.5$ aperture, 8.0 mm effective focal length, and M12 × 0.5 S mount.

3.5 Interfaces with Other Satellite Subsystems and Governing Software

It was decided to use a single microcontroller to operate both the camera and the motor so that this secondary OBC acted as an extension of the main OBC. Its only task was to collect data and activate actuators in the payload board. Meanwhile, the main OBC was the one deciding when to perform the individual tasks. In terms of communication protocol, I2C was implemented for the payload. Quetzal-1's software allowed it to operate the payload under either of two modes: autonomous or manual. Under autonomous mode, the satellite would take a picture and download it at a predetermined periodicity (which could be changed via a GCS command). Under the manual mode, pictures were taken exclusively at the moment of receipt of a GCS command requesting the satellite to acquire an image. Since the camera was initially placed between two light filters (protected from sunlight), the operation was to rotate 45 deg to set the first lens in front of the camera, take a picture and rotate 135 deg to cover the lens again. Meanwhile, the image was stored in a SanDisk Industrial Grade 8 GB micro SD card (ScanDisk, Cat. No. SDSDQAF3-008G-XI) for subsequent download. Hardware checks were done during this operation (see Fig. 9 in Appendix C), including the verification of current and voltage flags and confirmation of motor position, to ensure that a successful picture would be taken. A command to rotate the carousel without taking pictures was not considered and therefore not included.

3.6 Picture Capture, Download, and Use

The picture download process was considered a high-risk procedure because it involved the transmission of image files from the payload microcontroller to the OBC through the I2C main bus. This increased the risk of bus latch-ups due to potential bus collisions between the transmitted payload data and data coming from other subsystems, based on preflight testing observations. Due to time constraints—as these collisions were discovered close to the date of satellite handover to JAXA—no redundancy or watchdog safeguards were implemented for the I2C bus. Therefore, a bus latch-up could only be solved via an external reset caused by battery depletion in space. The download process was also considered of high risk because it involved a sudden increase in the power consumed by the transceiver (GOMSpace, Cat. No. AX100) during 1 to 4 min when transmitting pictures to the ground. The EPS was designed to be capable of providing this expected amount of power, but the sudden power peak could translate into unexpected failures. For these reasons, it was determined before handover that the automatic download mode of the payload subsystem was not going to be used on orbit, and that the picture and download process was going to be manually executed via GCS commands when the satellite passed over Guatemala.

If images of the Earth's surface were received, it would confirm that the team was successful in implementing this concept of operations, by developing and operating a carousel with light filters rotated via a piezoelectric motor, aligning a light filter to a sensor to acquire data at a specific wavelength. A picture would be needed to confirm this given that the carousel had

a default position where the sensor was covered by the solid aluminum block of the carousel, i.e., a light filter was not aligned to the sensor, with the intent of protecting it from direct sunlight. Should images of water bodies be received, these would be used to test the chlorophyll-a concentration algorithms after appropriate calibration, albeit this was limited with the last-minute sensor change as described in Sec. 3.3. Nevertheless, this was not a direct objective given our limitation to a passive ADCS, as described in detail by Alvarez et al.,[5] which would not allow for active targeting of lakes. This first mission would be focused in assessing whether this approach of multispectral imaging acquisition could be implemented in a 1U CubeSat.

4 Preflight Testing

An FEA of the payload's carousel was performed using simplified CAD model parts where bolts and holes were removed, since they were not necessary for the analysis. The body and filters materials were aluminum 7075 and optical glass, respectively. Given that the orientation of the satellite with respect to the launch vector was unknown, two different orientations were simulated. On the first scenario, a 177.5 m/s^2 acceleration vector was set on the $-Z$ axis, and this was set on the $+X$ on the second scenario (Fig. 5). With those settings, the modeled von Mises stress for the $-Z$ and $+X$ axis were 1.2053 and 8.9028 MPa, respectively. The safety factor was hand calculated based on the yield strength of aluminum 7075 (503 MPa) due to the software not providing a safety factor above 15, resulting in 417 and 56 safety factors for the $-Z$ and $+X$ axes, respectively.

Acceptance and characterization tests were performed on the lens, motor, and camera to compare their behavior against what was expected from their specification sheets and to understand their performance and limitations, respectively. The camera sensor and lens were tested to determine their focal length, distortion, and resolution. The focal length was determined by acquiring images at a given distance from a target, the horizontal distance covered by the sensor was compared against the horizontal size of the sensor in millimeters. The distortion was done by acquiring images of a checkerboard pattern for which the square dimensions were known in millimeters, a comparison was done between the actual dimension of the checkerboard pattern and the one obtained by measuring the image. Finally, the resolution was obtained by acquiring images of a fixed-sized target at different distances and comparing it to the amount of pixels that the target covered at each distance, and a linear relationship between distance and spatial resolution was obtained.

The piezoelectric motor was tested to characterize its rotational speed, positioning precision, and power consumption. The rotational speed of the motor varied according to the temperature at which it was operating, as well as the nature of the load that it needed to rotate. First, the motor (with no load) was subjected to four thermal cycles varying from −20°C to 60°C. Every time the temperature reached −20°C, 25°C, or 60°C, the motor was rotated a total of 15 times, and its angular speed was measured on each rotation. The average speeds of the motor at −20°C, 25°C, and 60°C were 157.5 ± 0.6 rpm (95% confidence interval), 134.4 ± 1.3 rpm, and 90.0 ± 1.3 rpm, respectively. This behavior can be explained from the nature that the piezoelectric crystal resonates differently as the temperature changes.[22] Additionally, a test was performed at room temperature (25°C) with the motor rotating the carousel filter, which had a mass of 0.143 kg and a total moment of inertia of 109.843 kg mm^2. The motor was rotated 15 times,

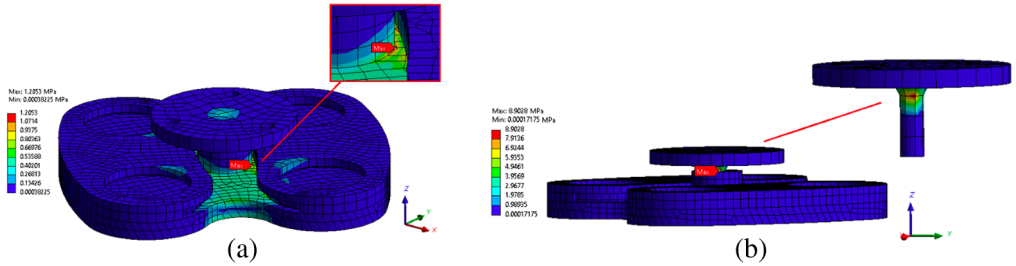

(a) (b)

Fig. 5 Von Mises stress with acceleration in (a) $-Z$ and (b) $+X$ during an $18.1 \times g$ launch acceleration.

and its average speed with a load was 125.73 ± 1.21 rpm. Finally, for the power consumption test, a current monitor was installed at the power input of the motor driver to quantify peak power consumption as the motor fully rotated the carousel 250 times. The average power demanded by the motor while it rotated was 4.34 ± 0.36 W, being the absolute maximum 5.13 W. On the other hand, the average power demanded by the motor while it was on but not rotating was 0.19 ± 0.02 W.

Preflight testing of image acquisition and processing by the OBC could only be performed on the last few weeks prior to handover due to the problems encountered with the sensor originally meant to be flown, as described in Sec. 3. These tests, however, were insightful in showing that there was a tendency for the I2C bus to hang, resulting in catastrophic and unrecoverable failure of the OBC. A correlation was observed of this happening with sometimes (not always) when an image was sent from the payload to the OBC, so it was hypothesized this was occurring due to data from other subsystems colliding with what the payload was sending to the OBC. To mitigate this risk, with only a matter of days before the satellite needed to move on the process towards handover, for the first flight the picture capture protocol was simplified to taking an image with the first light filter (445 nm) exclusively, and then returning to the "safe" position where the carousel would protect the sensor from sunlight.

A different type of the satellite's preflight testing was related to the launch vibration environment. As part of the project's mission assurance processes (see Ref. 3 for further details), a critical risk was identified regarding the payload's probability of failure during this test due to the use of glass on the light filters and on the camera lens. To mitigate this risk, a preliminary vibration test was performed on the payload alone while development work continued on the rest of the subsystems. With this approach, there would still be time to implement design modifications on the carousel if needed. This test took place at the Space and Planetary Exploration Laboratory at the University of Chile, Santiago de Chile, Chile. It was decided that for this test the payload should be exposed to the same vibration profile JAXA requested for the preflight tests of the satellite, with an overall acceleration value of 4.825 Grms in each axis for 1 min. The complete vibration profile provided by JAXA, as it was implemented in subsequent vibration tests of the whole satellite prior to handover, can be found in Table 2. A fixture was machined to hold the carousel via a bar mimicking the motor's shaft on one side, and to interface with the vibration table, on the other (see Fig. 6). Since the geometry of the carousel was symmetrical in the XZ and the YZ planes, only one test had to be performed to verify both the X and Y axes. Due to technical limitations found during the preliminary tests for the payload, it was not possible to achieve the overall value of 4.825 Grms. Instead, only 2.342 and 2.230 Grms overall were achieved on the X/Y and Z axes, respectively. The light filters were visually inspected at the end of the random vibration tests, showing no damage.

Preflight vibration tests of the assembled satellite were performed at the Higgs Centre for Innovation in Scotland using the values shown in Table 1. After the end of the test, a visual

Table 2 Random vibration profile implemented on Quetzal-1's payload subsystem at the Higgs Centre for Innovation, in Scotland.

Frequency (Hz)	PSD (G^2/Hz)
20	0.015
25.6	0.027
30	0.08
80	0.08
133.1	0.04
200	0.04
2000	0.002
Overall	4.825 Grms

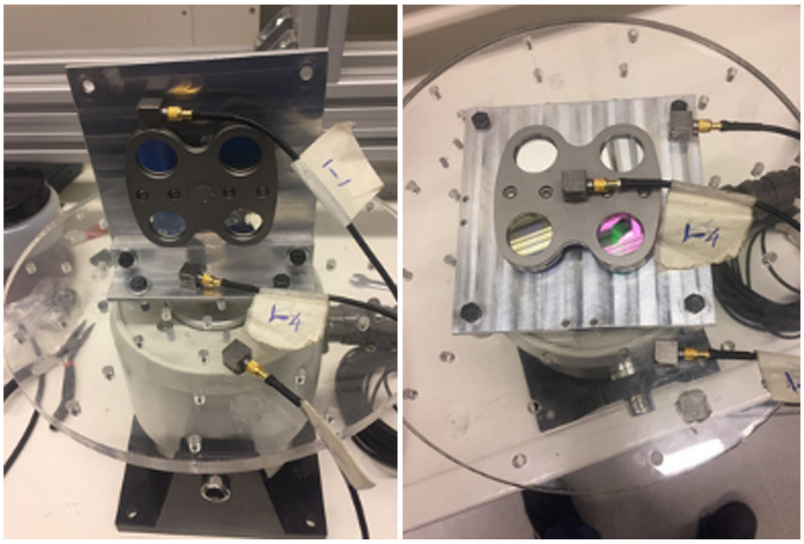

(a) (b)

Fig. 6 Carousel on Universidad de Chile's vibration table via a fixture: (a) X/Y axes testing and (b) Z axis.

inspection of the exterior of the satellite was performed to verify that none of the glass components had shattered or cracked. It was also verified that the screws holding the structure and the exterior plates did not loosen during the tests. After the visual inspections, it was concluded that the satellite did not suffer any damage during the tests and no screws loosened. Data acquired by accelerometers externally attached to the satellite during the test were used to verify the tests were performed according to the specifications.

5 Spaceflight Performance and Results

Quetzal-1 was successfully deployed from the Japanese Experiment Module Small Satellite Orbital Deployer attached to the Kibo module of the ISS on April 28, 2020 at 15:20:18 UTC. The first decoded beacon was received ~1 h later at 16:43:55 UTC, marking the start of the commissioning phase of the satellite. The commissioning phase lasted from deployment through June 2020 and did not yet include payload checks. Health data received from the satellite confirmed that the EPS subsystem was able to adequately harvest, store, and distribute the energy required for nominal operations on orbit.[4] The telemetry also confirmed that the ADCS had successfully detumbled the satellite, and that the average angle between the camera boresight and Nadir was 48.06 deg ±0.88 deg (99% CI) when the satellite was passing over Guatemala.[5] This angle was deemed adequate to capture pictures of the Earth's surface with the on-board camera, based on the payload's optical design (Sec. 3.4).

5.1 Revised Picture Capture and Download Protocol

After the commissioning phase of the mission, communication tests were performed to determine the most effective way of commanding the satellite during payload operations. It was determined that each command needed to be sent as a batch of six repeating command packets. This maximized the probability that the command would be successfully received by the omnidirectional antennas of the satellite. It was determined that passes with a maximum elevation >40 deg were adequate to execute picture capture and download processes. The satellite could be easily commanded at elevations >30 deg. At lower elevations, the communication link became irregular. A series of steps needed to be executed during payload operations to minimize the aforementioned failure risks. A pass with a +40 deg maximum elevation typically gave a 3-min window to execute this process. Table 4 (Appendix B) lists these steps and the rationale for their executions.

The watchdog reset timer that rebooted the OBC every 2 h ensured that the satellite always returned to its nominal configuration even if the reconfiguration commands sent after picture download were not successfully received by the satellite due to low elevation, or otherwise.

The value of the parameters modified during payload operations was only stored on the satellite's volatile RAM memory, thus they returned to their default values saved on the satellite's flash memory upon reboot. Furthermore, another safeguard was implemented to guarantee that the payload subsystem would not execute an automatic picture download if the subsystem was not successfully disabled after a payload operation. The payload's automode cycle time was permanently changed from 30 to 255 min (4 h and 15 min). The subsystem's time counter was reset to zero by the OBC's watchdog timer every 2 h. Therefore, the new cycle time ensured that the counter never reached 4 h and 15 min, triggering an automatic picture download.

5.2 Payload Performance Related to EPS and ADCS

The camera typically demanded 60 mA on standby mode when powered on during payload operations and demanded 195 mA when executing a picture capture and save, as detailed in Ref. 4. This corresponded to nominal operation of the camera, i.e., no differences were observed in the camera's per consumption with respect to preflight ground-based characterization tests. The carousel motor power consumption could not be evaluated because the power transient was too fast to be detected with the configured EPS sampling period. However, no short-circuit or overcurrent alert was triggered during any payload operation throughout the mission, evidencing the correct operation of the subsystem in space.[4] The piezoelectric motor rotated ~1812 times in space. This estimate was calculated by counting the times it rotated when it reconfigured itself to its 0 deg position after an OBC watchdog timer reset, and adding the successful payload operations detailed in the next section. A 2.41 W power consumption increase was measured when the transceiver (GOMSpace, Cat. No. AX100) downloaded an image.

As detailed in Ref. 5, the carousel generated a gyroscopic torque over the satellite when it rotated around the Z axis. This transient gyroscopic torque temporarily increased the satellite's oscillation over its X and Y axes. This in turn, increased the H-field oscillations on the satellite's hysteresis rods, thus providing rotational energy dampening. The carousel was activated during every OBC watchdog timer reboot because the motor was reset to its zero position. This phenomenon may have acted as a momentum dumping method that prevented a greater increase in rotational velocity over the satellite's uncontrolled axis. The effect of the rotations of the carousel caused by payload operations was negligible compared to the effect of the rotations caused by the watchdog timer reboots every 2 h.

5.3 Image Results

A total of 20 pictures were captured and 16 of those were downloaded. Five were all-black images due to reduced lighting during eclipse conditions, another five were all-white images showing little to no details, suggesting a potential limitation on the camera's AEC capabilities. To interrogate this aspect, subsequent image acquisition was timed on overflights of the GCS in Guatemala to take place during local sunrise or sunset. It was considered that this would provide more amicable lighting conditions to the sensor's AEC. However, the initial four of these pictures only showed out-of-focus lens flares caused by solar rays shining over the camera boresight. Finally, two pictures were captured at a time when the satellite was about to enter Earth's shadow and the planet's surface in front of the camera was slightly illuminated. This seems to have prevented the camera's sensor from being overexposed, allowing Quetzal-1 to capture images of hurricane Iota as it was impacting Guatemala (November 17, 2020 23:15 and 23:16 UTC) (see Fig. 7).

After analyzing the downloaded images, it was hypothesized that the time between carousel rotation to uncover the camera lens and the picture capture (50 ms) was not enough for the camera to automatically adjust its exposure and focus parameters according to lighting conditions. Unfortunately, the delay between these two steps was hard-coded into the payload software and could not be changed via GCS commands. The autoexposure and autofocus configuration of the camera was also hard-coded, thus these parameters could not be manually configured during the mission. Therefore, the payload operations relied on the lighting conditions during satellite passes over Guatemala to capture images. This proved to be a difficult task due to all the orbital conditions needed to guarantee the capture of a picture that was neither overexposed nor all dark.

These two images were captured during the same payload operation on November 17, 2020 at 23:15:11 UTC and 23:16:26 UTC, respectively. As observed in the pictures, the satellite was

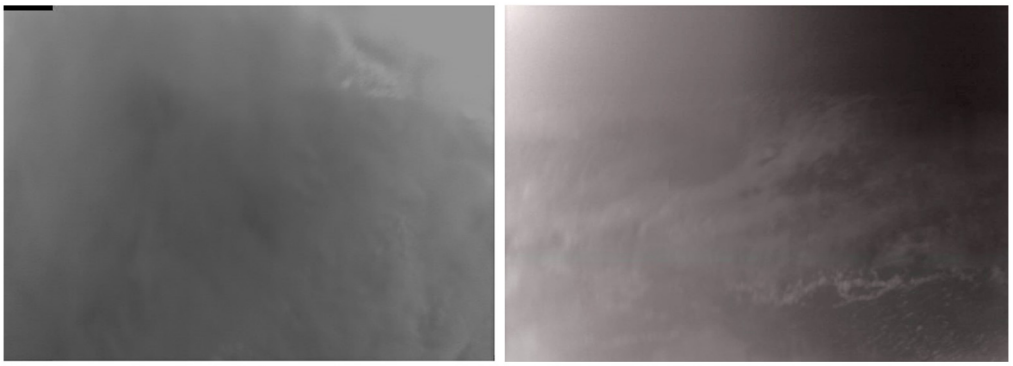

(a) (b)

Fig. 7 Image of Hurricane Iota over Guatemala and the Caribbean Sea, respectively, taken by Quetzal-1 with the 450 nm light filter on (a) 2020-11-17-231511 UTC and (b) 2020-11-17-231626 UTC.

aligned to Earth's terminator, which likely provided an adequate balance between illuminated and obscured surfaces. This allowed the camera to pick up details from clouds that were later determined to be part of hurricane Iota due to the location of the satellite when the pictures were captured.

5.4 Ground Sampling Distance Analysis for Hurricane Iota Pictures

A ground sampling distance (GSD) analysis—used to determine the distance between two pixels measured on the ground—was performed for the Hurricane Iota picture taken on November 17, 2020 at 23:16:26 UTC (16-UVG-2020-11-17-231626, Fig. 10 right). Quetzal-1's coordinates during the capture of image were 18.651° N, 86.228° W, 408.49 km, i.e., it was over the Caribbean Sea, 157 km to the east of the coast of Quintana Roo, Mexico. The GSD analysis was carried out taking into account the following characteristics of the payload's 5MP OV5642 image sensor and the M2508ZH02 lens: sensor height and width were 2738.4 and 3673.6 μm, respectively, the lens was a 1/2.5 in. 8.0 mm M12 × P0.5, with 8 mm focal length and 640 × 480 video graphics array (VGA) resolution. The GSD was calculated separately for the vertical and horizontal axes of the image following Eq. (5). For simplification, it was assumed that the camera's line of sight was perpendicular to the surface of the Earth at the time of the picture capture:

$$\mathrm{GSD}_{\frac{h}{w}} = \frac{\text{altitude (m)} \cdot \text{sensor height/width (mm)}}{\text{focal length (mm)} \cdot \text{image height/width (px)}}. \tag{5}$$

The resulting GSD for the horizontal axis was 291.30 m per pixel, and the GSD for the vertical axis was 293.09 m per pixel. This meant that, at a resolution of 640 × 480, the horizontal axis covered a total of 188 km and the vertical axis covered 140 km. Thus the picture of Hurricane Iota captured over the Caribbean Sea covered 26,228 km^2 of the Earth's surface.

5.5 End of Mission

Subsequent to the taking of the images in Fig. 7, the Quetzal-1 mission reached its end of mission due to battery failure following repeated subzero temperature exposures. Although the battery heaters showed appropriate performance during the life of the satellite, it is believed the OBC failed to command the heater to activate as a result of a Payload-OBC I2C bus hang, based on preflight testing as described in Sec. 3.6.

6 Discussion

Regardless of the application, for satellites with similar payloads to Quetzal-1's, piezoelectric motors are ideal due to their lack of magnets and lubricants, as this makes them amicable with passive ADCS and optical surfaces, respectively. This also helps acquire images at multiple wavelengths in a small volume, which may not be needed in larger satellites but can be helpful in smaller systems like a 1U CubeSat. This manuscript includes the engineering drawings of the carousel parts; teams are encouraged to modify it, as it may house five or more filters by

reorganizing it or choosing smaller diameter light filters (e.g., those commonly used on benchtop photometers).

From the programmatic perspective and in hindsight, there are three essential lessons learned from aspects that could have gone better during the mission: (i) the payload and its operation need to be identified first to generate clear requirements for the rest of the subsystems, (ii) plan for more testing time (per satellite system, integrated, and day-in-the-life), for subsequent modifications, iterations, and more testing prior to handover than what would seem to be necessary, and (iii) consider using hardware that has no flight heritage only if it can be delivered with enough time that would allow for its testing, and potential change should it not meet the satellite's and mission's needs. In the case of Quetzal-1, the payload was not identified first due to personnel limitations, and this caused otherwise unnecessary complications. Similarly, implementing a new sensor so close to handover was possible in part to the open-source nature of the hardware and software (both from Arduino® and its community). Above and beyond, the lesson learned from this project is that a motivated group of students, with some guidance and resources, can achieve the unimaginable: despite no precedent space projects or local know-how in the country, Quetzal-1 was developed by a team of ∼100 people 21 years of age in average, who were mostly undergraduate students as there are no graduate engineering programs in the country. Part of the success is also attributable to the advice received from advisers who volunteered their time. Finally, literature surveys on what has and has not worked on previous missions is a valuable tool, for which we hope this paper will serve other teams and encourage them, especially in institutions in developing countries, to develop their own spaceflight missions for resource management and other peaceful applications.

7 Conclusions

1. TEKCELEO's WLG-30 piezoelectric motor performed without any recorded off-nominal incidents in space, and hence may be considered by other teams as an option given this flight heritage.
2. Arduino's Arducam OV5642 camera performed without any recorded off-nominal incidents in space, and hence may be considered by other teams as an option given this flight heritage.
3. Anodizing the carousel in black helped minimize glare and the risk of cold welding of the carousel to other structural components contacting the rotating system.
4. The rotating carousel system induced a gyroscopic torque on the spacecraft due to the misalignment between the carousel's rotating axis and the spacecraft's angular momentum vector. Nevertheless, no adverse impact of this gyroscopic torque was observed in the science data.
5. Regarding preflight testing, performing vibration tests on the carousel housing the glass light filters proved ideal for programmatic risk mitigation in a timely fashion, i.e., at a point in the project where changes could still have been made, which would have not been the case if a problem with the glass parts would have been found during integrated vibration tests prior to hand over.
6. Science data downlink via UHF transmissions proved to be inefficient and a limiting factor in the amount of science data that could be obtained during the mission.
7. The inability to manually change the camera settings via ground command proved to be a limiting factor in the amount of science data obtained during the mission due to the automatic white balancing and exposure time issues experienced on orbit, which caused most of the downlinked pictures to turn out completely white.

8 Recommendations

1. Given that glare of the camera lens reflecting on the light filters was observed in pictures taken on orbit it is recommended that the satellite's shell is designed to minimize places where light may enter and reflect on internal components. Similarly, it is recommended that the orifice on the nadir-facing surface of the satellite (to allow for image acquisition) be as small as possible for the same reason.

2. Given the challenges encountered with downlinking images via UHF transmissions due to the limited data rate, the authors recommend the use of other frequency bands, such as S-Band or X-Band, which provide higher data rates and increased data budget margins for image acquisition missions.
3. Due to technology demonstration nature of this mission, spatial and temporal resolutions were not drivers on sensor selection but must be considered by those designing a fully functional mission. Nevertheless, for other watercolor monitoring missions, placing an 800 nm bandpass filter instead of the 700 nm implemented on Quetzal-1 may also enable the implementation of a normalized differential vegetation index algorithm and exclude CDOM.
4. In addition to the characterization tests mentioned in Sec. 4, it is strongly recommended that the sensor(s) that will be used on the flight article be tested and calibrated using drones or airplanes over the mission targets. This will enable to take *in situ* data to correlate to the data produced by the sensor(s), hence allowing for a faster transition from the commissioning to the fully operational mission phase. These preliminary tests should produce as deliverable a confirmation that the images in each wavelength can be taken and saved quickly enough so that they can be co-registered.
5. It is recommended that a command to rotate the carousel without taking pictures be included, as well as to change the duration between carousel rotation and image acquisition for commissioning and calibration purposes prior to science data collection.
6. It is also recommended that the satellite be able to receive ground commands to change sensor and camera settings, including exposure time, autofocus, shutter speed, and white balance for calibration purposes.

9 Appendix A: Summary of Space Borne Sensors for Chlorophyll-A Sensing

Table 3 provides a non-exhaustive literature survey on sensors used, in part, for chlorophyll a characterization, previously or currently used on space platforms.

Table 3 Summary of space borne sensors used for chlorophyll-a measurements, based on Ref. 9.

Sensor	Spacecraft	Operator	Resolution (km)	Bands	Wavelength range	Numerator	Denominator	Source
CZCS	Nimbus-7	USA	0.8	4	443 to 670	443	520 or 550	Hu and Campbell[9]
SeaWiFS	Orbview-2	USA	1.1	8	412 to 865	443, 490, or 510	555 (and 670 for 3-band algorithm)	Hu and Campbell[9] and Hu et al.[11]
MODIS	Terra/Aqua	USA	1.1	9	412 to 869	443 or 488	547	and Hu and Campbell[9]
MERIS	Envisat-1	Europe	1.2	12	413 to 865	443 or 490	560	Hu and Campbell[9]
OCM-1/2	IRS-P4	India	—	8	402 to 885	—	—	IOCCG[10]
GOCI	COMS	South Korea	0.5	8	412 to 865	—	—	IOCCG[21]

CZCS, coastal zone color scanner; SeaWiFS, Sea-viewing wide field-of-view sensor; MODIS, moderate resolution imaging spectroradiometer; MERIS, medium resolution imaging spectrometer; OCM, ocean color monitor; GOCI, geostationary ocean color imaged; VIIRS, visible infrared radiometer suite.

10 Appendix B: Visual Representation of Key Optical Parameters

Figure 8 visually describes the key optical parameters described in Sec. 3.4.

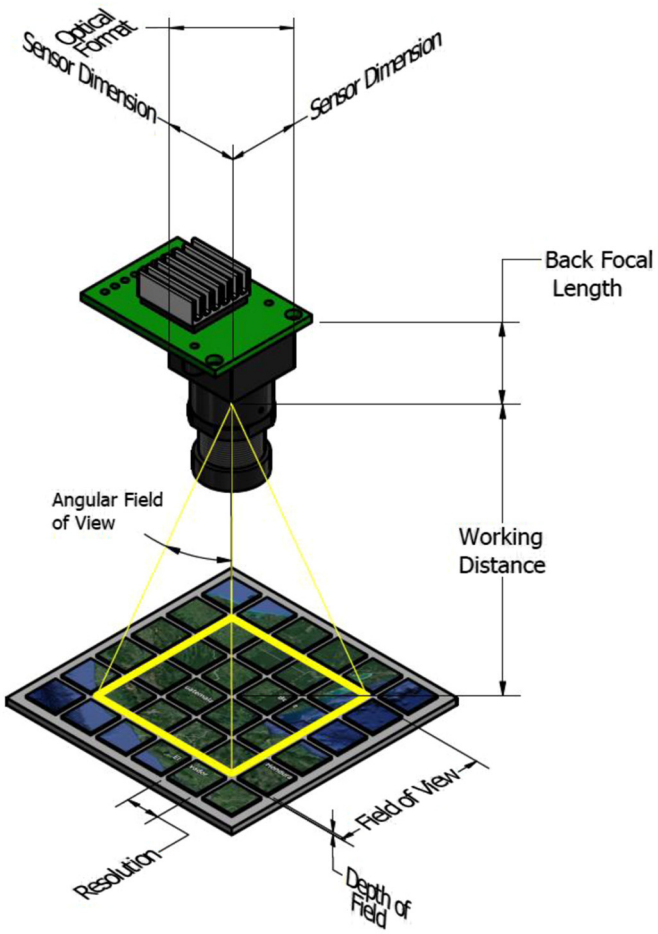

Fig. 8 Visual representation of key optical parameters.

11 Appendix C: Payload Operation Command Sequence

Table 4 and Fig. 9 describe the algorithm implemented for manual and automatic image capture, respectively.

Table 4 Steps and commands executed during manual image capture and download operations (informed by space-based results during commissioning phase).

Step no.	Description	Rationale for execution
1	Change the battery temperature sampling period from 30 to 240 s via GCS command	Cleared the I2C bus from any transaction between EPS and OBC that did not involve the payload subsystem's activation for 4 min
2	Wait for beacon confirmation of the change	—
3	Enable the payload module via GCS command	This step allowed the software to enter the picture capture and download subroutine when commanded
4	Wait for beacon confirmation of the change	—
5	Change the beacon cycle time from 10 s to 255 s via GCS command	Reduced the frequency of beacons to further clear the I2C bus from any transaction external to the payload subsystem
6	Wait 15 s to confirm that beacons are suspended	—
7	Send the command for payload basic operation	Executed picture capture and picture download
8	Wait for picture capture and download to be completed	—
9	Disable the payload module via GCS command	Prevented the software from executing another payload operation
10	Reconfigure battery temperature sampling time to 30 s and the beacon cycle time to 10 s via GCS commands	Returned the satellite to its normal configuration after payload operation

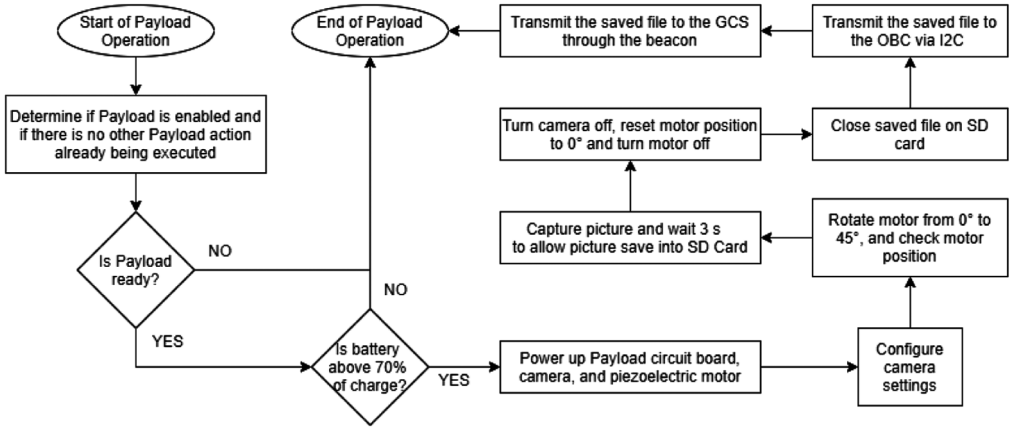

Fig. 9 Automatic picture capture and download flow diagram.

12 Appendix D: Carousel Engineering Drawings

In the spirit of helping other teams with similar academic and technical objectives, we have made the Quetzal-1 code and engineering drawings openly available. In this appendix through Figs. 10–12 we present the engineering drawings of the components of the payload carrousel.

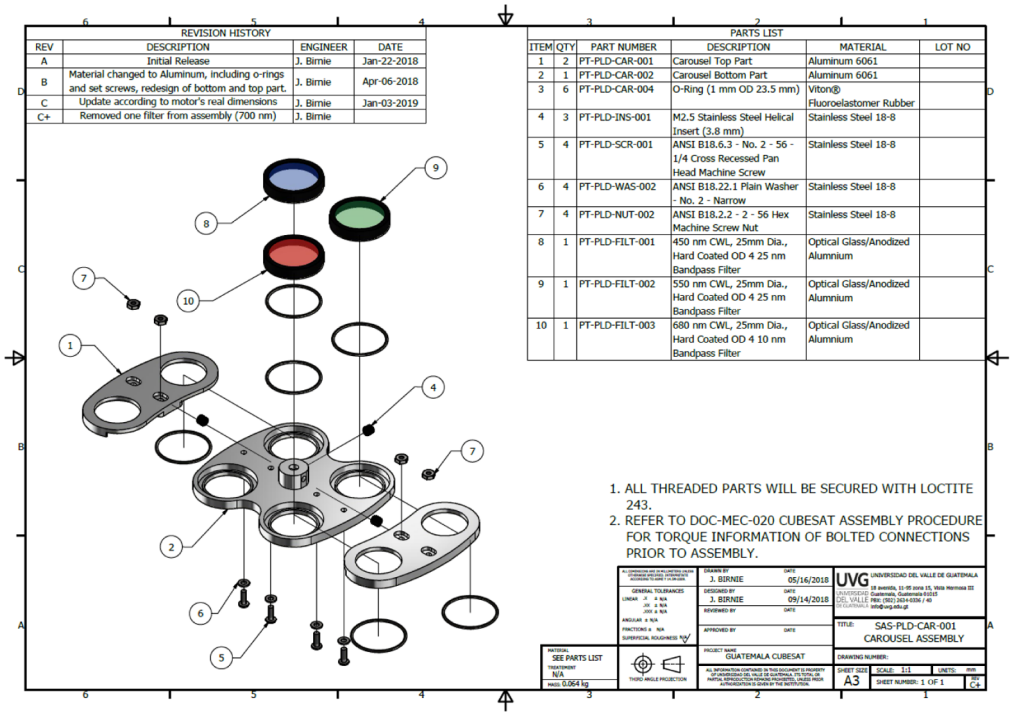

Fig. 10 Carousel assembly drawing.

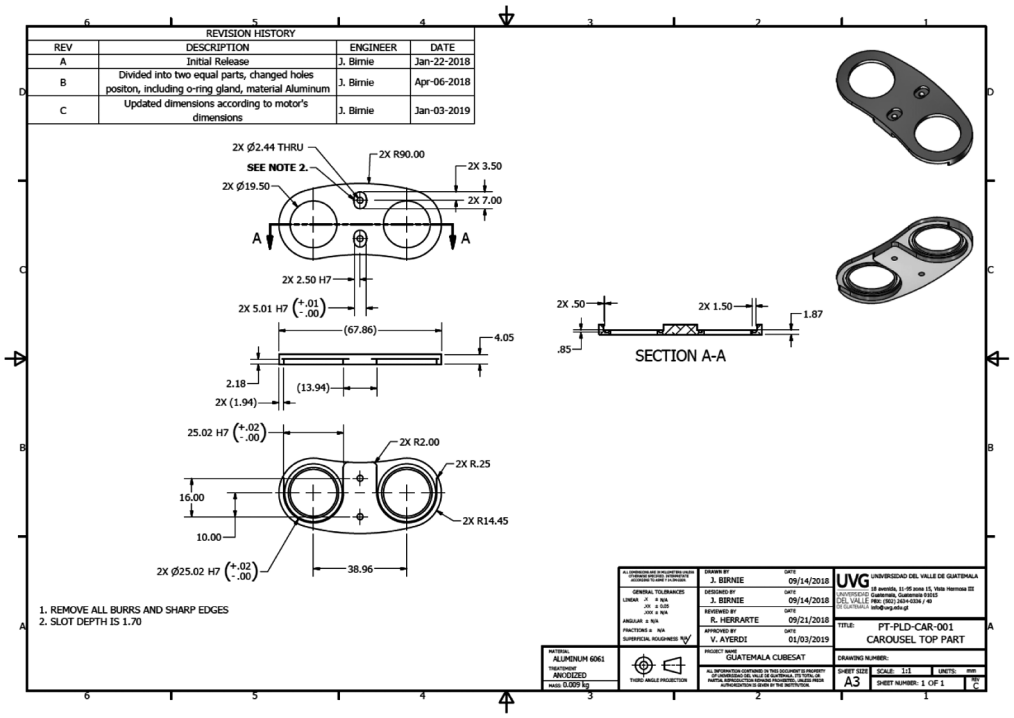

Fig. 11 Carousel top part drawing.

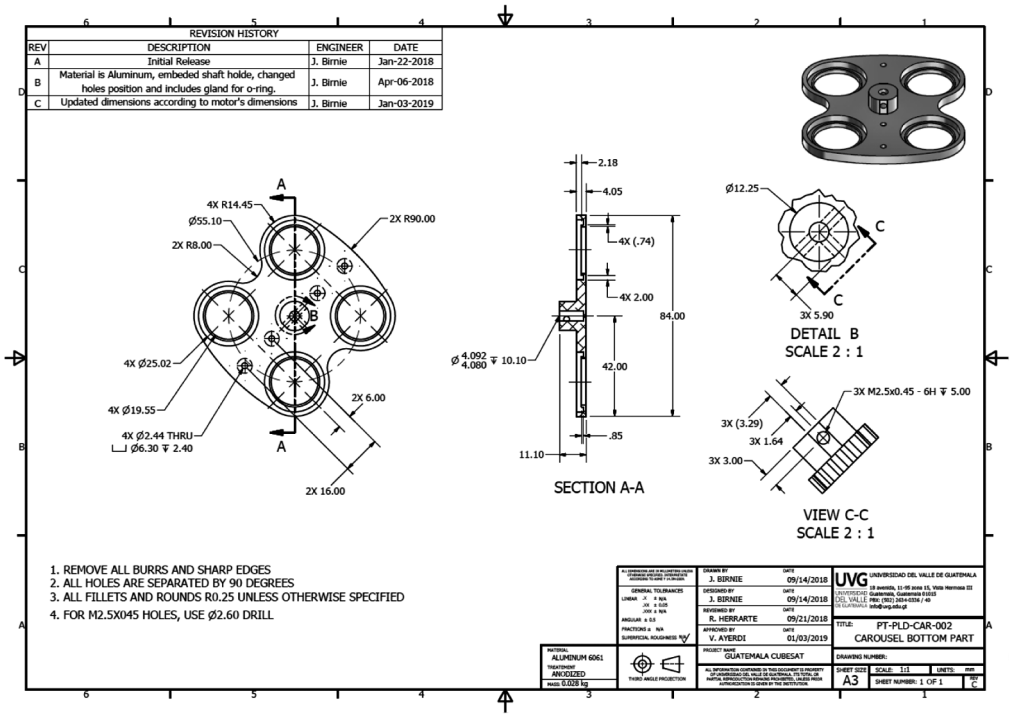

Fig. 12 Carousel bottom part drawing.

Code and Data Availability

The data presented in this paper are publicly available in GitHub at https://github.com/Quetzal-1-CubeSat-Team/quetzal1-telemetry.

Acknowledgments

The authors would like to thank the Universidad del Valle de Guatemala for its support, which made this project possible. CubeSat safety reviews and launch and deployment from the ISS were provided under KiboCUBE, a joint program of the United Nations Office for Outer Space Affairs and Japan Aerospace Exploration Agency. Environmental testing was done thanks to the support of United Kingdom Space Agency and ASTROSAT. The authors would like to acknowledge the Universidad de Chile's Space and Planetary Exploration Laboratory and the Laboratory of Mechanical Vibrations and Rotordynamics specifically to Mr. Julian Barra, Mr. Gustavo Díaz, Mr. Elias Obreque, Dr. Viviana Meruane, and Dr. Marcos Díaz for the vibration test of the light filter carousel performed in their facilities. Anodisa is thanked for their anodizing of the carousel and Grupo SSC (Mexico) and ANSYS® for their technical support and providing the license to make the simulations. Prof. Sebastian Schmidt is thanked for his expert insight as external adviser, especially during the conception of Quetzal-1 payload, and for reviewing this paper. Ivan Castro is also thanked for his expert advice on photography and for reviewing this paper. We also would like to thank África Flores for her guidance during the bandwidth selection process. Quetzal-1 advisers are thanked and acknowledged, including África Flores, Dr. Andrew Dahir, Dr. Chantal Cappelletti, Dr. David Gerhardt, Erick Tijerino, Iván Castro, Dr. James Mason, Julia Stalder, Dr. Julio Edgar Gallegos Alvarado, Marco Escalante, Dr. Sebastian Schmidt, Prof. Scott Palo, and Prof. Sergio Montenegro. Quetzal-1's payload was designed by UVG undergraduate students, and this manuscript is possible thanks to their work in different capacities to make the hardware a reality. This group of students includes Sergio Argueta, José Antonio Muñoz, Santiago Solórzano, Roberto Rossino, Juan Pablo Cahueque, Cesar Saavedra, and Hugo Elvira. UVG's Prof. José Rodrigo Aragón is thanked for serving as internal reviewer and adviser, and Carlos Morales is thanked for his work and support manufacturing the carousel.

References

1. L. Zea et al., "A methodology for CubeSat mission selection," *J. Small Satell.* **5**(3), 483–511 (2016).
2. F. Taniguchi, H. Akagi, and K. Matsumoto, ""KiboCUBE"—UNOOSA/JAXA cooperation program for capacity building by using the innovative CubeSat launch opportunity from ISS "Kibo,"" in *Space Capacity Building in the XXI Century*,S. Ferreti, Ed., pp. 85–94, Springer, Cham (2020).
3. M. Martínez et al., "Guatemala's remote sensing CubeSat—tools and approaches to increase the probability of mission success," in P*roc. 32nd Annu. AIAA/USU Conf. Small Satell.*, Logan, Utah, pp. 1–10 (2018).
4. A. Aguilar-Nadalini et al., "Design and on-orbit performance of the electrical power system for the Quetzal-1 CubeSat," *J. Small Satell.* **12**(2), 1201–1229 (2023).
5. D. Alvarez et al., "Design and on-orbit performance of the attitude determination and passive control system for the Quetzal-1 CubeSat," *J. Small Satell.* **12**(2), 1231–1247 (2023).
6. JAXA, "JEM Payload Accommodation Handbook—Vol. 8—Small Satellite Deployment Interface Control Document (JX-ESPC-101133-B)," 2015, http://aerospacebiz.jaxa.jp/wp-content/uploads/2016/07/jem_handbook_eng.pdf (accessed 23 Nov. 2021).
7. NASA, "Materials and processes technical information system (MAPTIS)," 2023, https://maptis.nasa.gov (2021).
8. L. A. Mertes et al., "Rivers and lakes," in *Manual of Remote Sensing: Remote Sensing for Natural Resource Management and Environmental Monitoring*,S. L. Ustin, Ed., pp. 345–400, Wiley, Hoboken, New Jersey (2004).
9. C. Hu and J. Campbell, "Oceanic chlorophyll-α content," in *Biophysical Applications of Satellite Remote Sensing*,J. Hanes, Ed., Springer, Berlin Heidelberg, pp. 171–203 (2014).
10. International Ocean Colour Coordinating Group (IOCCG), "Ocean Colour Monitor (OCM) on Indian Remote Sensing Satellite IRS-P4," 2015, http://www.ioccg.org/reports/ocm/ocm.html (accessed 23 Nov 2021).
11. C. Hu, Z. Lee, and B. Franzz, "Chlorophyll-α algorithms for oligotrophic oceans: a novel approach based on three-band reflectance difference," *J. Geophys. Res.* **117**, C01011 (2012).
12. H. J. Gons et al., "Optical detection of cyanobacterial blooms," in *Harmful Cyanobacteria*,H. Matthijs and P. M. Visser, Eds., pp. 177–199, Springer, Dordrecht (2005).
13. UVG, "Quetzal-1 CubeSat," 2021, https://www.uvg.edu.gt/cubesat-en/ (accessed 26 Nov. 2021).
14. J. Lee, "Manual exposure for OV2640: ArduCam," 2017, https://www.arducam.com/manual-exposure-ov2640/#:~:text=The%20OV2640%20Timing&text=Given%20the%20pixel%20clock%20is,pixels%20and%20dummy%20lines%20added (accessed 23 Nov. 2021).
15. W. G. Rees, *Physical Principles of Remote Sensing*, 3rd ed., Cambridge University Press, Cambridge (2012).
16. Edmund Optics Inc., "Understanding focal length and field of view," 2017, https://www.edmundoptics.com/resources/application-notes/imaging/understanding-focal-length-and-field-of-view/ (accessed 9 July 2017).
17. Videology, "Depth of field," http://www.videologyinc.com/support-lens-handbook-pg3.htm (accessed 8 July 2017).
18. A. Babu, "Choosing the right lens for e-CAM50_CU5642_MOD custom lens camera module - part1," http://www.e-consystems.com/Articles/Product-Design/choosing_custom_lens_camera.asp (accessed 23 Nov. 2021).
19. Nikon, "Camera basics," 2021, https://imaging.nikon.com/lineup/dslr/basics/13/ (accessed 23 Nov. 2021).
20. Qimaging, "Rolling shutter vs. global shutter," 2014, https://www.photometrics.com/learn/white-papers/rolling-vs-global-shutter (accessed 28 July 2017).
21. International Ocean Colour Coordinating Group (IOCCG), "Geostationary Ocean Color Imager (GOCI)," 2014, http://www.ioccg.org/sensors/GOCI.html (accessed 23 Nov. 2021).
22. T. Van Dam, *Dynamic Analysis of a Piezoelectric Ultrasonic Motor*, http://resolver.tudelft.nl/uuid:bfebf616-592f-4c53-82ad-71635eb328b8 (2011).

Biographies of the authors are not available.